Fuel 403 (2026) 136088

Contents lists available at ScienceDirect

Fuel

journal homepage: www.elsevier.com/locate/fuel

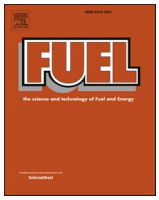

Full Length Article

Aerobic oxidation of 5-Hydroxymethylfurfural to 2,5-Furandicarboxylic acid over Au/Hydrotalcite catalyst – role of support and synthesis methodology on the activity and stability

Ane Bueno [a,*], Nerea Viar [a], Matthew B. Conway [b], Inaki Gandarias [a], Jesús M. Requies [a], Meenakshisundaram Sankar [b,*]

[a] Chemical and Environmental Engineering Department, Bilbao School of Engineering, University of the Basque Country (UPV/EHU), Plaza Ingeniero Torres Quevedo 1, Bilbao 48013, Spain
[b] Cardiff Catalysis Institute, Translational Research Hub, School of Chemistry, Cardiff University, Maindy Road, Cardiff CF24 4HQ, UK

ARTICLE INFO

Keywords:
FDCA
Supported Au nanoparticles
Hammett titration
Magnesium leaching
Deactivation mechanism
Reaction mechanism

ABSTRACT

The oxidation of 5-hydroxymethylfurfural (HMF) to 2,5-furandicarboxylic acid (FDCA) is key in producing bio-based plastics like polyethylene furanoate (PEF), a sustainable alternative to petrochemical materials. This work reports a systematic study on how the hydrotalcite (HT) support precursors—specifically using Na^+ or NH_4^+ precursors and the choice of synthesis method (deposition–precipitation, DP, or sol immobilization, SI) influence the catalytic performance and stability of Au/HT catalysts under base-free reaction conditions. Au/HT_{Na} DP achieved 100 % HMF conversion and FDCA yield without an external base. This high activity is reflected in its turnover frequency (TOF), reaching 12.1 h^{-1} per basic site and 287.4 h^{-1} per gold site. The superior performance of Au/HT_{Na} DP is attributed to the strong synergy between gold nanoparticles (AuNPs) and weak basic sites (OH^- groups) of the HT, whose abundance is dictated by the choice of precursor. In contrast, Au/HT_{NH4} SI, despite higher Au dispersion, showed lower activity due to reduced basicity. Magnesium leaching was identified as the primary cause of catalyst deactivation, and a regeneration strategy employing $Mg(OH)_2$ was developed to successfully restore both the structure and basicity of the catalyst. These findings offer practical insights into the design of recyclable, base-free catalytic systems for sustainable FDCA production.

1. Introduction

The transition from fossil-derived to bio-based chemicals is critical in addressing global challenges such as climate change, resource depletion, and plastic pollution [1]. Bioplastics like polyethylene furanoate (PEF), derived from renewable resources, offer a sustainable alternative to conventional plastics, potentially transforming industries reliant on petrochemical feedstocks [2].

In this context, 2,5-furandicarboxylic acid (FDCA) has gained significant interest in the chemical industry as a bio-based renewable substitute for terephthalic acid (TPA) in the synthesis of bio-based plastics, such as PEF [3,4]. The efficient and selective oxidation of 5-hydroxymethylfurfural (HMF) to FDCA, using environmentally benign oxidants, is essential for advancing sustainable materials and reducing reliance on fossil resources [5–7]. The synthesis of FDCA from HMF involves the selective oxidation of the alcohol and aldehyde groups in HMF to form the desired diacid (see **Scheme S1**) [8]. Two main pathways are reported: In the first pathway, the oxidation of the hydroxyl group to 2,5-diformylfuran (DFF) and then to FDCA via 5-formyl-2-furancarboxylic acid (FFCA); whereas, in the second pathway, the aldehyde group oxidizes to 5-hydroxymethyl-2-furancarboxylic acid (HMFCA), followed by sequential oxidations to FDCA via FFCA [9,10].

The use of O_2 or air as oxidants in FDCA production offers both economic and environmental advantages, aligning with green chemistry principles [11]. In addition to these oxidants, recent studies have explored alternative systems, such as the use of NaClO as an oxidant for

* Corresponding authors at: Department of Chemical and Environmental Engineering, Bilbao School of Engineering, University of the Basque Country (UPV/EHU), Plaza Ingeniero Torres, Quevedo 1, Bilbao 48013, Spain, Cardiff Catalysis Institute, Translational Research Hub, School of Chemistry, Cardiff University, Maindy Road, Cardiff CF24 4HQ, UK.
E-mail addresses: ane.bueno@ehu.eus (A. Bueno), nerea.viar@ehu.eus (N. Viar), conwayM2@cardiff.ac.uk (M.B. Conway), inaki.gandarias@ehu.eus (I. Gandarias), jesus.requies@ehu.eus (J.M. Requies), sankar@cardiff.ac.uk (M. Sankar).

https://doi.org/10.1016/j.fuel.2025.136088
Received 3 April 2025; Received in revised form 21 May 2025; Accepted 22 June 2025
Available online 28 June 2025

HMF oxidation to FDCA, which has shown high activity in aqueous media when combined with non-noble metal catalysts like CuO_x-CoO_y heterostructures on graphene [12]. Noble metals (such as Au, Pt, Pd, and Ru) remain widely employed due to their superior ability to activate molecular oxygen and catalyze selective oxidations [13–15]. These metals exhibit varied catalytic abilities: gold exhibits higher activity for aldehyde group oxidation (see **Scheme S2**), while platinum, ruthenium and palladium are more effective for alcohol group oxidation [16–20]. These differences are influenced by the type of metal and the structural properties of the catalyst, such as metal particle size and dispersion [21,22]. For example, Au/CeO_2 (2.6 wt%) achieved nearly 100 % FDCA yield under mild conditions [23], whereas 1.6 wt% Au/ZrO_2 reached 89 % yield under elevated temperature while Au/ZrO_2 (1.6 wt%) reached 89 % yield at higher temperatures [24]. Similarly, Pt/$Ce_{0.8}Bi_{0.2}O_{2-\delta}$ gave a 98 % FDCA yield in just 0.5 h [25], and PVP-stabilized Pd nanoparticles achieved a 90 % yield under moderate conditions [26]. In contrast, ruthenium catalysts generally exhibit lower efficiencies; for instance, Ru/Al_2O_3 yielded only 63 % FDCA [27].

Despite these high yields, the catalytic oxidation of HMF to FDCA typically requires the addition of external homogeneous bases, such as NaOH, Na_2CO_3, or $KHCO_3$, to facilitate intermediate formation and product solubility [28–30]. For example, a study on Pd-Au nanoparticles supported on Mg-Al hydrotalcite showed that bimetallic catalysts with varying Pd/Au ratios performed well for the oxidation of HMF to FDCA in an alkaline aqueous solution, achieving a high yield of FDCA (90 %) with the addition of NaOH [31]. Similarly, in the selective oxidation of HMF to HMFCA over Ag–PVP/ZrO_2 catalysts, $Ca(OH)_2$ was found to outperform NaOH and Na_2CO_3 in promoting HMFCA formation under mild conditions, underscoring the critical role of base selection in intermediate yield and reaction efficiency [32]. However, this reliance on bases introduces significant challenges, including increased production costs, generation of inorganic salt by-products, and environmental concerns [33,34]. Strong alkaline conditions, sometimes requiring up to 20 equivalents of NaOH [35], further intensify operational challenges due to corrosion and elevated material costs.

To overcome these limitations, research groups have explored the use of basic supports like hydrotalcite (HT), a layered double hydroxide with abundant surface OH^- groups. HT has shown promise for supporting metal nanoparticles and preventing aggregation of basic salts. However, its stability is compromised under acidic conditions, as magnesium leaching occurs due to the acidic nature of FDCA (pKa = 2.28) [36]. This issue necessitates the addition of excess HT to maintain basicity during the reaction [37]. Strategies to address these challenges include optimizing the Mg/Al molar ratio in HT to enhance basicity and performance [38], using bimetallic catalysts such as PdPt-PVP/HT to eliminate the need for added bases [39], and employing synergistic supports like HT-activated carbon composites to improve activity and stability compared to conventional Au/HT or Au/AC systems [40,41].

Despite these advancements, gaps remain in understanding the influence of HT characteristics and preparation methods on catalytic activity and stability. For example, the calcination temperature of HT significantly affects its structure and basicity, altering catalytic behavior [42]. In glycerol oxidation, Au/HT catalysts calcined above 373 K showed increased activity, but the product distribution varied compared to other Au catalysts, highlighting the impact of preparation methods on reaction pathways [43]. Moreover, the particle size of Au on HT and its interaction with the support can influence both activity and stability [44].

The biphasic system, consisting of an organic (i.e. methyl isobutyl ketone (MIBK)) and an aqueous phase, was chosen to mitigate secondary degradation reactions of HMF, which are prevalent in aqueous media [45]. This approach builds upon our previous work [46], where we demonstrated that the use of MIBK as the organic solvent significantly improved the yield of HMF from fructose, and was essential for the subsequent oxidation to FDCA. The current study focuses on optimizing the catalytic activity of the Au/HT catalysts, investigating how the composition of the HT support and catalyst preparation methods affect the activity and stability. Special emphasis is placed on the role of HT precursors (Na^+ and NH_4^+) and synthesis methods (deposition–precipitation and sol immobilization) in determining, gold dispersion, and basicity. Based on these findings, a reaction mechanism is proposed, which helps understanding the effect of deactivation on catalyst's activity and selectivity. Furthermore, the most efficient catalyst, capable of achieving a 100 % FDCA yield without an added base, can be regenerated through a simple method that restores its activity and selectivity.

2. Material and methods

2.1. Materials

The following reagents were used for the experiments: HMF (98 %), HMFCA (95 %), FFCA (98 %) and FDCA (98 %), were purchased from Sigma-Aldrich. The following solvent were used for the experiment: MIBK (99 %) purchased from Sigma-Aldrich. The following reagents were used for the catalyst preparation: $HAuCl_4{\cdot}3H_2O$ (99 %), NH_3 (25 %), $Mg(NO_3)_2{\cdot}6H_2O$ (99 %), $Al(NO_3)_3{\cdot}9H_2O$ (99 %), $Na_2CO_3{\cdot}10H_2O$ (99.5 %), NaOH (99 %), $(NH_4)_2CO_3$ (98 %), NaH_4OH (97 %), PVA (99 %), $NaBH_4$ (97 %), $PdCl_2$ (98 %) and TiO_2 (99.5 %) were purchased from Sigma-Aldrich. Gold 1 % on zinc oxide granulate (AUROlite™ Au/ZnO) catalyst was purchased from Strem Chemicals, Inc. All chemicals were used without further purification.

2.2. Catalyst preparation

Synthesis of Mg/Al = 5 hydrotalcite with Na (HT_{Na}): Following Gupta et al. [42] procedure, HT_{Na} with a Mg/Al ratio of 5 was synthesized by mixing 0.5 M $Na_2CO_3{\cdot}10H_2O$ and 1.167 M NaOH solution with 0.5 M $Mg(NO_3)_2{\cdot}6H_2O$ and 0.1 M $Al(NO_3)_3{\cdot}9H_2O$ solution. The first solution was added dropwise to the second solution until a pH of 10 was reached. The solution was heated at 65 °C for 3 h. The resulting gel was filtered, washed to pH 7, and dried 16 h at 110 °C.

Synthesis of Mg/Al = 5 hydrotalcite with NH_4 (HT_{NH4}): HT_{Na} with a Mg/Al ratio of 5 was synthesized by mixing 0.5 $(NH_4)_2CO_3$ and NaH_4OH/H_2O (1:1 in volume) solution with 0.5 M $Mg(NO_3)_2{\cdot}6H_2O$ and 0.1 M $Al(NO_3)_3{\cdot}9H_2O$ solution. The first solution was added dropwise to the second solution until a pH of 10 was reached. The solution was heated at 65 °C for 3 h. The resulting gel was filtered, washed to pH 7, and dried 16 h at 110 °C.

Synthesis of Au/HT_X by deposition–precipitation method (Au/HT_X DP): Using the deposition–precipitation method [47], 0.1 mmol $HAuCl_4$ was dissolved in 40 ml water with 1 g HT. Ammonia solution (NH_3, 25 %) was added to reach pH 10, followed by stirring for 6 h and refluxing for 30 min at 100 °C. The solid was then filtered, washed to pH 7, and dried at 110 °C 16 h, followed by a heat treatment at 200 °C for 4 h.

Synthesis of Au/HT_X catalyst by sol immobilization (Au/HT_X SI): Using the sol immobilization method [48], an aqueous solution of the metal precursor $HAuCl_4{\cdot}3H_2O$ (2.5 mM) was added to 140 ml of water. Then, 2.5 ml of 22.7 mM concentrated PVA was added to the solution. Subsequently, a freshly prepared 5 ml of $NaBH_4$ solution (0.1 M) was added immediately to the solution, forming a sol. After stirring the mixture for 30 min, 1 g of the support material (HT_X) was added to the colloidal solution with stirring to facilitate the immobilization of the metal nanoparticles. After 3 h, the solid catalyst was recovered by filtration and washed with distilled water until a neutral pH of 7 was achieved. Finally, the catalyst was dried at 110°C for 16 h.

Synthesis of Au/TiO_2 catalyst by sol immobilization: Following Ahlers et al. [49] procedure, an aqueous solution of the metal precursor $HAuCl_4{\cdot}3H_2O$ (2.5 mM) was added to 140 ml of water in a 500 ml glass beaker. Then, 2.5 ml of 22.7 mM concentrated PVA was added to the solution. Subsequently, a freshly prepared 5 ml of $NaBH_4$ solution (0.1 M) was added immediately to the solution, forming a sol. After stirring

the mixture for 30 min, 1 g of the support material (TiO_2, P25,) was added to the colloidal solution with stirring. 2 drops of concentrated HCl was added to facilitate effective immobilization of the metal nanoparticles to the support surface. After 3 h, the solid catalyst was recovered by filtration and washed with distilled water until a neutral pH of 7 was achieved. Finally, the catalyst was dried at 110°C for 16 h.

Synthesis of Pd/HT_{NH4} catalyst by sol immobilization (Pd/HT_{NH4} SI): The procedure used for the synthesis of this material is similar to that listed in the previous section. However, for the synthesis of this catalyst, Au and Pd colloids were prepared separately. The metal precursors were combined with analogous quantities of PVA and reduced with an analogous quantity of $NaBH_4$, in separate beakers. Once the colloids had been synthesized, they were combined into one beaker and the desired quantity of support was immediately added. After 3 h of ageing, the solid catalyst was recovered by filtration and washed repeatedly with 500 ml distilled water to remove Na^+, BH_4^- and BO_2^-. Finally, the catalyst was dried at 110°C for 16 h.

2.3. Characterization

Specific surface area: Textural properties were obtained from the N_2 adsorption–desorption isotherms at − 196°C using an Autosorb iQ3 (Quantachrome, USA). Prior to measurements, samples were outgassed at 100°C for 8 h under vacuum to remove trapped moisture and other volatile species. Surface areas were calculated by the BET method.

X-ray diffraction (XRD) studies: X-ray diffraction patterns of the Au/HT catalysts were acquired to study the hydrotalcitic structure using a PANalytical® X'Pert PRO apparatus. X-rays were generated by a copper anode (K_α 1.54184 Å). The samples were scanned between 2θ angles of 10 and 80° with a step size of 0.008°.

Inductively coupled plasma (ICP) studies: The samples for leaching studies were run on an Agilent 7900 ICP-MS with I-AS autosampler with platinum sampling and skimmer cones, concentric nebulizer and quartz double pass spray chamber. All analyses were run using helium (He mode) and the ORS cell to reduce interferences. For metal content determination in solids, ca. 2 mg of catalyst was dissolved in 10 ml aqua-regia for at least 12 h. The final solution was diluted to 50 ml with water in a volumetric flask. In all cases, further dilutions were done if required. All results were done in duplication and further analyses were performed if two results differed.

X-ray photoelectron spectroscopic (XPS) studies: Elemental analysis and atom oxidation states of the Au/HT catalyst surfaces were performed on a Kratos Axis Ultra DLD photoelectron spectrometer utilizing a monochromatic Al *Kα* X-ray source operating at 140 W (10 mA x 14 kV). Data was collected with pass energies of 160 eV for survey spectra, and 40 eV for the high-resolution scans with step sizes of 1 eV and 0.1 eV respectively. For analysis, samples were either pressed on to doubled silicon free sided Scotch tape (type 665). The system was operated in the Hybrid mode, using a combination of magnetic immersion and electrostatic lenses and acquired over an area approximately 300 × 700 μm^2. A magnetically confined charge compensation system was used to minimize charging of the sample surface, and all spectra were taken with a 90° take of angle. A base pressure of ~ 5 × 10^{-9} Torr was maintained during collection of the spectra. Data was analyzed using CasaXPS (v2.3.26) after subtraction of a Shirley background and using modified Wagner sensitivity factors as supplied by the manufacturer.

Hammett titration method: The basicity of the HT and Au/HT catalyst were assessed using the Hammett titration method. 0.05 g of sample was dispersed in H_2O (10 ml) and stirred for 30 min to ensure uniform dispersion. Hammett indicators with known pKa values—bromothymol blue (pKa=7.2) and phenolphthalein (pKa=9.6)—were used to evaluate the basicity. 1 ml of the indicator solution was added to the catalyst suspension. After the addition of the indicator, titration was performed using benzoic acid (0.1 mM) under continuous stirring. The color change of the indicator was monitored visually to determine the neutralization of basic sites on the catalyst, corresponding to the pKa of the indicator used.

Scanning transmission electron microscopy (STEM) studies: Elemental maps for the samples were obtained to calculate the mean particle size of the catalysts. On the one hand, a FEI Titan Cubed G2 60–300 transmission electron microscope at 300 kV was used, equipped with a Schottky X-FEG field emission electron gun, a monochromator, and a CEOS GmbH spherical aberration (Cs) corrector on the image side. On the other hand, a Super-X EDX system was used under a high-angle annular dark-field (HAADF) detector for Z-contrast imaging under STEM conditions (camera length of 115 mm) using a pixel size of 2 nm, a dwell time of 900 s, and an image size of 512 × 512 pixels. In addition, EDX microanalyses were carried out with a Super-X EDX system, using a probe current of 240 pA and a semi-convergence angle of 10 mrad. HAADF STEM images were collected with an inner detector radius of 63.5 mrad.

Particle size distribution histograms were generated by analysis of representative HAADF electron micrographs using ImageJ (version 1.53f51). Additionally, the dispersion (D) of the catalysts, expressed as the percentage of active metal atoms exposed on the surface, was calculated using equation (1):

$$D = \frac{N_m \cdot S \cdot M}{100 \cdot L} \quad (1)$$

where N_m is the number of metal atoms on the surface per particle (mol/m^2), S represents the surface area occupied by a single metal atom (in m^2/g), M is the molecular weight of the supported metal (g/mol), and L is the percent metal loading of the supported catalyst.

Fourier Transform Infrared Spectroscopy (FT–IR): FT–IR spectra were recorded using a Bruker Vertex 70 spectrophotometer equipped with a Golden Gate Single Reflection Diamond ATR accessory, enabling analysis of solid samples without prior preparation. Spectra were collected in the mid-infrared region (4000–500 cm^{-1}) using a standard spectral resolution of 4 cm^{-1}. Each spectrum was obtained by averaging 64 scans to improve the signal-to-noise ratio.

2.4. Catalytic activity and product analysis

The experimental procedures involved conducting catalytic reactions within a 50 mL glass colaver® reactor. Initially, a solution containing 0.1 g HMF in a 10 ml MIBK/H_2O solvent mixture at a volume ratio of 3:1 was prepared and introduced into the reactor. Subsequently, the catalyst (170 mg) was suspended in the solution. The glass reactor underwent three oxygen purges and was adjusted to maintain a pressure of 3 bar consistently throughout the experiment, ensuring continuous replenishment of oxygen as it was consumed during the reaction. The reaction mixture was heated to 95°C and stirred for the specified duration. After the reaction period, the reactor vessel was cooled in an ice bath for 10 min. Once cooled, the reactor was opened, and the two resulting phases were separated via decantation. Following the completion of the oxidation stage and the decantation of the aqueous phase, Na_2CO_3 was added at a 3:1 M ratio (salt/HMF) to dissolve FDCA in water and facilitate its quantification. The resulting solution was centrifuged for 3 min at 3000 rpm to separate the catalyst from the solution.

Analysis of the aqueous and organic phases was performed using High-performance liquid chromatography (HPLC) (HPLC 1260 Infinity equipped with a Hi-Plex H column, an infrared detector (RID), and a diode-array detection (DAD)). The conversions/yields of HMF, levulinic acid, and formic acid were determined using RID, whereas the yield of FFCA, DFF, HMFCA, and FDCA were measured using DAD with λ = 254. The HPLC parameters included a mobile phase of 10 mM H_2SO_4, a column temperature of 35°C, and a flow rate of 0.6 mL/min. Equations (2) and (3) were utilized to calculate the conversion of HMF and the yield of the products. The turnover frequency (TOF) was also calculated to evaluate the catalytic activity of the samples, considering both the

basic sites (4) and the Au active sites (5):

$$X_i\ (\%) = \frac{N_i^{t=0} - N_i^{t=t}}{N_i^{t=0}} \cdot 100 \quad (2)$$

$$Y_j\ (\%) = \frac{N_j^{t=t}}{N_i^{t=0}} \cdot 100 \quad (3)$$

$$TOF_{OH^-basic\ sites} = \frac{N_i^{t=0} - N_i^{t=t}}{N_{OH^-basic\ sites} \cdot t} \quad (4)$$

$$TOF_{Au\ active\ sites} = \frac{N_i^{t=0} - N_i^{t=t}}{N_{Au\ active\ sites} \cdot t} \quad (5)$$

where, *i* denotes HMF, while *j* represents FDCA, FFCA, HMFCA, or DFF, *N* stands for the mole quantity and *t* is the reaction time.

2.5. Au/HT_{Na} DP catalyst regeneration

This procedure involved preparing a saturated solution of $Mg(OH)_2$ in 20 mL of distilled water, from which 10 mL were taken and mixed with 0.25 g of the used catalyst. The mixture was stirred at 500 rpm for 3 h and 30 min at room temperature to promote the reintroduction of magnesium into the catalyst structure. Afterward, the catalyst was filtered, thoroughly washed with distilled water to remove any residual $Mg(OH)_2$, and dried at 100°C for 16 h to restore its activity and stability.

3. Results and discussion

3.1. Catalytic activity

Fig. 1**a** shows the catalytic activity of different catalysts in the oxidation of HMF to FDCA under identical reaction conditions, while the selectivity values are summarized in **Table S1**. The tested materials include gold-based catalysts supported on hydrotalcite (Au/HT), prepared via deposition–precipitation (DP) and sol-immobilization (SI) methods, as well as Pd/HT synthesized via sol-immobilization for comparison. For comparison, Au/TiO_2 and a commercial Au/ZnO catalyst were also tested for the reaction under identical reaction conditions. Additionally, a combination of the commercial Au/ZnO catalyst co-fed with $Mg(OH)_2$ was tested to examine the influence of adding a homogeneous base to the reaction system.

Hydrotalcite-supported gold catalysts exhibit significantly higher catalytic performance, both in terms of HMF conversion and FDCA yield, compared to the non-hydrotalcitic catalysts. These results suggest that the basic nature of the HT might play a key role in the reaction mechanism. Among these, the Au/HT_{Na} DP catalyst achieved complete HMF conversion with 100 % FDCA yield. The catalyst preparation method played an important role, as seen in the differences between DP and SI methods. For Au/HT_{Na}, the DP method significantly outperformed SI, with the latter showing lower FDCA yield and substantial formation of intermediates. Conversely, for Au/HT_{NH4}, the SI method exhibited better performance compared to DP, although neither achieves complete HMF conversion or FDCA yield. Therefore, the choice of HT precursor and the synthesis method strongly influence catalytic behavior.

In contrast, Au/TiO_2 and commercial Au/ZnO catalysts displayed moderate activity, with HMF conversions of 29.8 % and 34.5 %, respectively, and FDCA yielded below 15 %. Significant amounts of intermediates remained unconverted, highlighting the limited efficiency of these supports. The addition of $Mg(OH)_2$ to Au/ZnO improved both HMF conversion (51 %) and FDCA yield (18.6 %), indicating that increased basicity in the aqueous medium enhances the reaction, but yet significantly below the results obtained with Au/HT_{Na} DP and Au/HT_{NH4} SI. The Pd/HT catalyst, despite being supported on hydrotalcite, showed lower activity and selectivity than its gold-based equivalents. This emphasizes the suitability of gold as the active metal in this reaction system, particularly when paired with a hydrotalcitic support.

Overall, the findings confirmed the central role of hydrotalcite as a support in enhancing activity of gold-based catalysts for the HMF oxidation reaction and the catalyst synthesis procedure. Next, characterization results are shown to understand how the choice of the hydrotalcite precursor (Na or NH_4) and gold incorporation method (DP or SI) affects the structure–activity relationship of Au/HT catalysts.

3.2. Catalyst characterization

The Au/HT materials were characterized using BET surface area analysis, XRD, XPS, ICP, STEM and Hammett titration method. The textural properties of the catalysts are summarized in **Table S2**. The HT_{Na} exhibited a moderate surface area, which decreased slightly after Au deposition via deposition–precipitation, indicating minor pore blockage due to the presence of AuNPs. In contrast, the SI method led to a drastic reduction in surface area and a significant increase in pore diameter, suggesting partial structural collapse or severe pore obstruction. This loss of structural integrity may account for the significantly lower catalytic performance of Au/HT_{Na} SI, which showed reduced HMF conversion and FDCA selectivity compared to its DP counterpart. In the case of the HT_{NH4}–based catalysts, both DP and SI methods preserved similar pore sizes and volumes, although the SI method resulted in a slightly lower surface area. Notably, Au/HT_{NH4} SI exhibited substantially higher FDCA selectivity and conversion than Au/HT_{NH4} DP, which correlates with the greater accessibility and dispersion of AuNPs observed in the SI catalyst. These findings highlight that the catalyst preparation method plays a critical role in preserving or disrupting the porous structure of the support, ultimately influencing the accessibility of active sites and, therefore, the overall catalytic activity.

The XRD patterns of the synthesized HT and Au/HT materials are shown in Fig. 1**b-c.** All materials displayed the characteristic diffraction peaks of layered double hydroxides (LDH), corresponding to the (003), (006), (009), (015), (018), (110), and (113) planes (ICDD-PDF no. 00–041–1428) [50]. No additional crystalline phases were detected, indicating high phase purity of the HT and Au/HT samples. Notably, after the incorporation of Au nanoparticles onto HT, no diffraction peaks corresponding to Au were observed in the XRD patterns of the Au/HT catalysts. This absence suggests either a high dispersion of Au nanoparticles or their size being below the XRD detection limit (4 nm). The results confirm that the LDH structure of the HT support was preserved after the addition of Au nanoparticles, regardless of the choice of precursor or the gold incorporation method.

The surface composition of the catalysts was analyzed using XPS. Fig. 1**d-g** presents the high-resolution spectrum of the gold 4f core level. This spectrum is characterized by two distinct pairs of peaks, corresponding to the spin–orbit coupling of Au $4_{f7/2}$ and Au $4_{f5/2}$ [51,52]. The spectral analysis indicates partial oxidation of the gold surface. Specifically, the first and most prominent pair of peaks, with binding energies of 83.6 eV and 87.3 eV, corresponds to elemental gold (Au^0), while the second pair is associated with gold in the + 1 oxidation state (Au^{1+}), or more likely small Au particles at MgO defect sites [53] with binding energies of 85.1 eV and 88.8 eV [54,55]. Additionally, magnesium and aluminum were also detected on the surface, confirming the presence of these elements from the support material. No peaks associated with Au^{3+} were detectable. **Table S3** presents the surface atomic percentages (At. %) for each element on the surface of the catalysts.

For the Au/HT_{Na} DP catalyst, the surface concentration of Au^0 was relatively low (0.56 %), with a minor presence of Au^{1+} (0.07 %). Despite this, the catalyst achieved exceptional performance, with complete HMF conversion and 100 % FDCA yield. This suggests that an abundance of metallic gold on the surface is not strictly required to achieve high catalytic activity, likely due to synergistic effects between the gold species and the hydrotalcitic support. In contrast, the Au/HT_{Na} SI catalyst exhibited a significantly higher surface concentration of Au^0 (2.59 %) and Au^{1+} (0.25 %), yet its catalytic performance was lower,

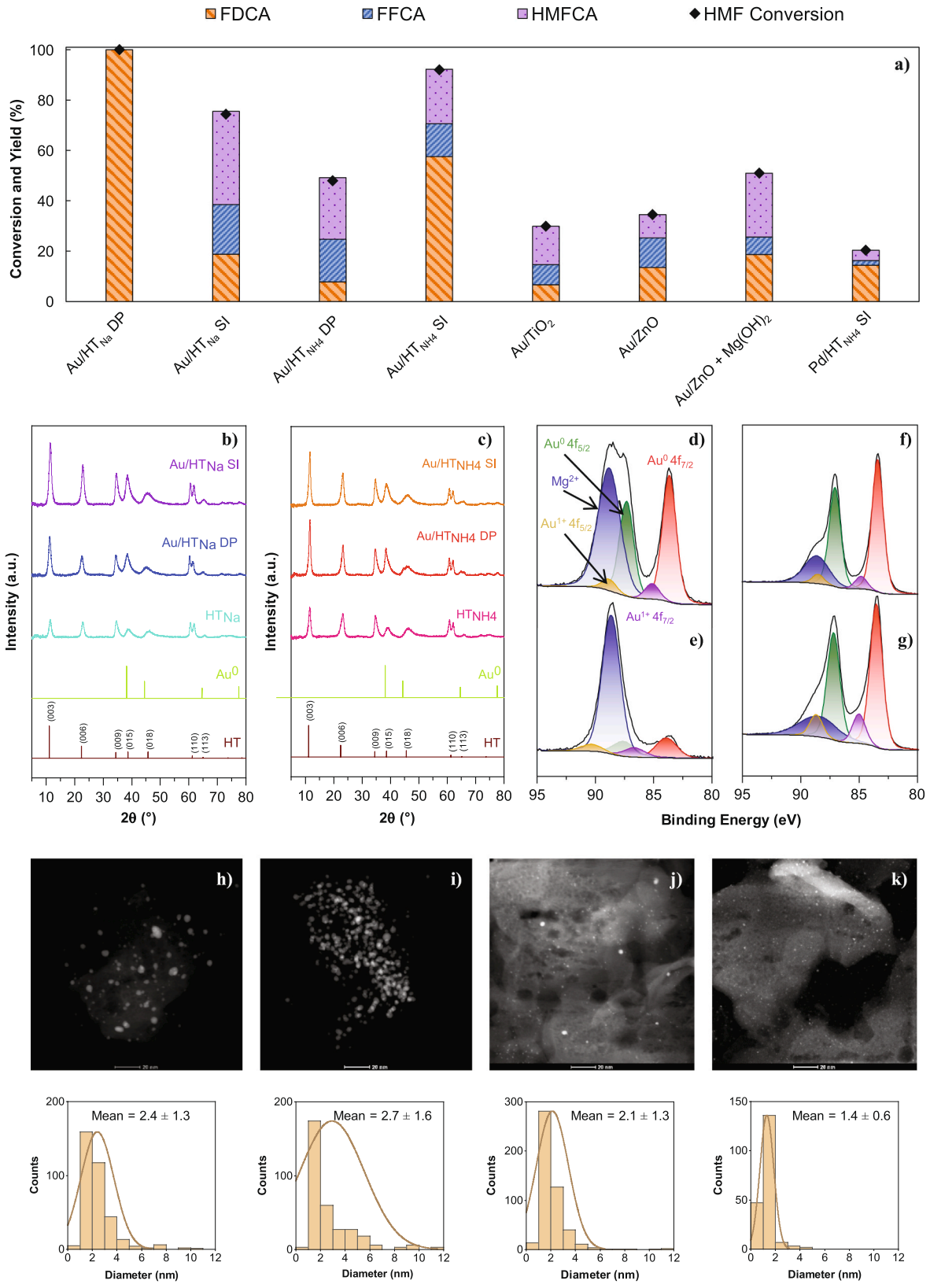

Fig. 1. **a)** Catalytic activity of HMF oxidation into FDCA. Reaction parameters: 3 bar (O_2), 95°C, 500 rpm, 0.1 g HMF, 10 ml of total liquid phases, MIBK/H_2O volume ratio = 3:1, 18 h, 0.17 g catalyst. XRD patterns of **b)** HT_{Na} based catalysts and **c)** HT_{NH4} based catalysts. XPS spectra of **d)** Au/HT_{Na} DP, **e)** Au/HT_{NH4} DP, **f)** Au/HT_{Na} SI, and **g)** Au/HT_{NH4} SI catalysts. TEM images and particle size distribution of **h)** Au/HT_{Na} DP, **i)** Au/HT_{Na} SI, **j)** Au/HT_{NH4} DP and **k)** Au/HT_{NH4} SI catalysts.

with only 18.8 % FDCA yield. When using an NH_4^+–based hydrotalcite precursors, the surface composition and catalytic performance differ further. The Au/HT_{NH4} DP catalyst showed the lowest Au^0 content (0.17 %) and a similarly low concentration of Au^{1+} (0.08 %). The Au/HT_{NH4} SI catalyst demonstrated the highest surface concentrations of both Au^0 (4.02 %) and Au^{1+} (0.82 %), along with the highest Mg^{2+} content (24.39 %). This catalyst achieved 92 % HMF conversion and a moderate FDCA yield of 57.55 %. The XPS results highlight that SI method consistently leads to higher surface concentrations of metallic gold (Au^0) compared to the DP method. In the SI method, colloidal AuNPs are formed *ex situ* through the reduction of $HAuCl_4$ with $NaBH_4$ in the presence of polyvinyl alcohol (PVA). This approach promotes the formation of well-reduced gold clusters [48,56]. By contrast, in the DP method, gold is precipitated *in situ* onto the hydrotalcite surface [57].

To explore the influence of the preparation method on the size of gold nanoparticles (AuNPs), HT–based catalysts were characterized using TEM. Fig. 1**h-k** presents the TEM images and corresponding particle size distributions of the four catalysts, while EDS elemental mapping in **Fig. S1** illustrates the spatial distribution of Au, Al, and Mg within the same catalysts. The following trend in average AuNPs size was observed: Au/HT_{NH4} SI < Au/HT_{NH4} DP < Au/HT_{Na} DP < Au/HT_{Na} SI. This result suggested that the SI method favors the formation of smaller nanoparticles compared to the DP method when NH_4^+–based precursors were used. However, the catalytic activity does not follow a direct correlation with particle size alone. As shown in **Fig. S2a**, no clear trend was observed between Au dispersion and FDCA yield, reinforcing the idea that additional factors play a crucial role in determining catalytic activity. Moreover, the EDS mapping in Fig. 1**h-k** corroborated the TEM results, clearly showing well-dispersed and small AuNPs in the catalysts. Additionally, Mg and Al are homogeneously distributed in all samples, which is characteristic of hydrotalcite-like structures observed in the XRD analysis.

While the SI method coupled with NH_4^+–based precursors achieved the highest AuNPs dispersion and Au^0 surface concentrations, the catalytic results show that this is not sufficient to ensure high activity and selectivity. Therefore, other catalytic properties, like basicity, might play a critical role in the reaction mechanism. To this end, the Hammett titration method was employed to characterize the basicity of the catalysts.

Both the HT precursor and the preparation method significantly influence the quantity and strength of these basic sites (see **Table S4**). The basicity assessment revealed no color change with the 2,4-dinitroaniline (pKa=15) indicator, suggesting the absence of strong basic sites. In contrast, color changes were observed with phenolphthalein and bromothymol blue, confirming the presence of weak and medium basic sites. Particular emphasis was placed on the weak basic sites, which are directly associated with the surface OH^- groups [58]. For the HT_{Na} precursor, the fresh material displayed a total basicity of 1.42 mmol/g, with a high content (0.81 mmol/g) attributed to weak basic sites. After incorporating gold via DP, the basicity of Au/HT_{Na} DP decreased slightly to 1.17 mmol/g, and the contribution of weak basic sites dropped to 0.58 mmol/g. This reduction suggests that the DP method partially blocks the support's original basic sites, probably due to the interactions between the gold species and the weak sites.

Regarding the effect of the preparation method on the total basicity, the following trend as observed: Au/HT_{Na} DP > Au/HT_{NH4} DP > Au/HT_{NH4} SI > Au/HT_{Na} SI. This result indicates that the DP method is more effective than the SI method in preserving weak and medium basic sites on the catalyst. However, similar to Au dispersion, no direct correlation was found between the total amount of basic sites and catalyst activity. Interestingly, when focusing on weak basic sites, a strong linear relationship between the yield of FDCA and the quantity of weak basic sites was observed (**Fig. S2b**). Hence, it seems that these surface OH^- groups are the active ones in the reaction mechanism.

Collectively, the characterization of the Au/HT catalysts revealed that the basicity of the hydrotalcite support—especially the abundance of weak basic sites—was a critical factor in determining catalytic activity. The DP method generally preserved these basic properties more effectively than the SI approach, although the choice of hydrotalcite precursor influenced the final basicity profile.

To further elucidate the activity of the catalysts, the turnover frequencies (TOFs) of the two most active samples—Au/HT_{Na} DP and Au/HT_{NH4} SI—were obtained at similar conversion values (**Table S5**). The Au/HT_{Na} DP catalyst reached these conversions (i.e. 18 %) after the same reaction time but using nine times lower catalyst loading than Au/HT_{NH4} SI. While Au/HT_{NH4} SI exhibited higher Au dispersion, the Au/HT_{Na} DP catalyst benefited from a much higher density of OH^- basic sites, which likely enhanced reactant activation. This synergy led to substantially higher TOF values when normalized by either the number of basic sites (12.1 h^{-1}) or the gold sites (287.4h^{-1}), underscoring that the superior performance of Au/HT_{Na} DP arose not only from gold dispersion but also from the synergy with the weak basic sites of the HT support. A literature comparison (**Table S6**) [23,24,28,59–66] shows that most monometallic Au catalysts achieving similar HMF conversion and FDCA yield require stoichiometric or excess soluble base and higher O_2 pressures; in contrast, both Au/HT_{Na} DP and Au/HT_{NH4} SI deliver comparable performance under base-free conditions, highlighting the critical role of support basicity in substituting for homogeneous base addition.

3.3. Reaction mechanism proposal

In the next sections, a detailed reaction mechanism for the three step oxidation of HMF to FDCA using Au/HT catalysts is proposed. This mechanism integrates the roles of AuNPs, surface hydroxyl groups, oxygen, and water.

3.3.1. Oxidation of HMF to HMFCA

Initially, HMF adsorbs on a surface hydroxyl group, by interacting with the electrophilic carbon of the aldehyde group (–CHO) (Fig. 2**a)** [11]. This interaction leads to the formation of a hydroxylated intermediate (–$CH(OH)_2$) [23], which is stabilized on the catalyst surface (Fig. 2**b**).

Subsequently, the oxidation of this intermediate occurs. AuNPs activate O_2 through electron transfer [67,68], generating reactive oxygen species (ROS). The simultaneous hydride elimination in the hydroxylated intermediate by the ROS (Fig. 2**b-I**), and the nucleophilic attack of the hydroxyl ion (Fig. 2**b-II**) facilitate its transformation into a carboxylic acid (–COOH), leading to the formation of HMFCA. This mechanism is supported by the experimental data (**Table S7**), which show that oxygen is essential for the conversion of HMF to HMFCA. In the absence of O_2 (**Table S7**, entry 2), minimal HMF conversion is observed, while the presence of oxygen (**Table S7**, entry 1) significantly enhances transformation. Water stabilizes the intermediates, provides hydroxide ions and facilitates HMFCA desorption from the catalyst surface [38]. In contrast, when the reaction is performed in MIBK, there is almost no reaction due to the lack of hydroxide ions and because the HMFCA molecule has difficulty desorbing from the hydrotalcite surface, preventing the oxidation reaction from proceeding (**Table S7**, entry 3).

As observed in **Table S7**, entry 2, in the absence of oxygen, water can minimally oxidize HMF, converting it into HMFCA. Therefore, the role of AuNPs may extend beyond O_2 activation, potentially promoting water activation and generating hydroxide ions that drive oxidation [69]. The absence of HMF conversion (**Table S7**, entry 7) further supports this hypothesis, as HT alone is unable to activate either O_2 or water efficiently.

3.3.2. Conversion of HMFCA to FFCA

The second step involved the oxidation of the hydroxymethyl group (–CH_2OH) in HMFCA to an aldehyde group (–CHO), producing FFCA. Initially, the carboxylic acid group of HMFCA interacts with a hydroxyl groups present on the catalyst surface (Fig. 2**d**). Previously shown

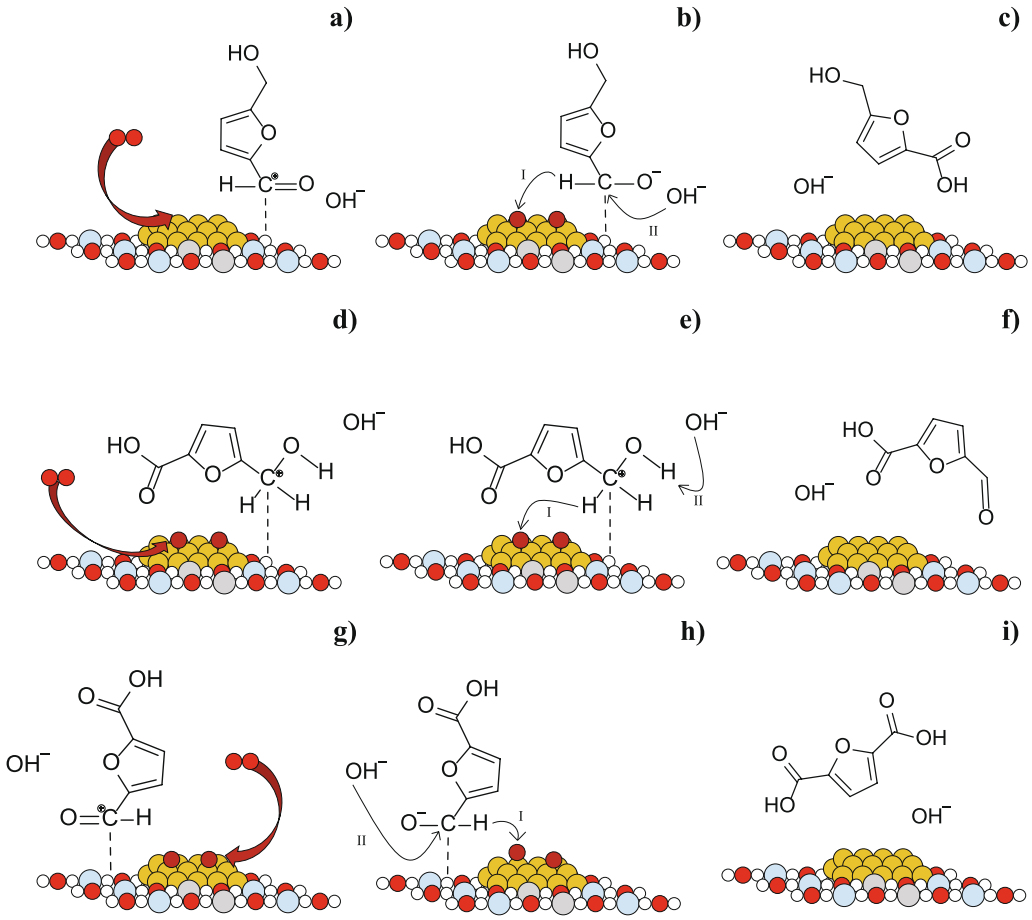

Fig. 2. Proposed reaction mechanism for the oxidation of HMF to FDCA over Au/HT catalysts. White spheres represent H^+, red spheres O^{2-}, dark red spheres O_2*, blue spheres Mg^{2+}, gray spheres Al^{3+}, and yellow spheres Au. (For interpretation of the references to color in this figure legend, the reader is referred to the web version of this article.)

activity (Table S1) and characterization data supports this mechanism: while the Au/TiO_2 catalyst—lacking significant surface OH^- groups—shows an accumulation of HMFCA (≈50 % selectivity), the HT-based catalysts follow a similar trend. In fact, HMFCA selectivity follows the order Au/HT_{Na} DP < Au/HT_{NH4} SI < Au/HT_{Na} SI < Au/HT_{NH4} DP, which is the inverse of the trend observed for surface hydroxide group concentration via Hammett analysis. This inverse relationship suggests that higher HMFCA selectivity means the reaction slows down at this intermediate stage. The lack of surface hydroxyl sites makes it harder for HMFCA to adsorb onto the catalyst, preventing its further oxidation. Once adsorbed, ROS generated by AuNPs induces a β-hydride elimination (Fig. 2**e-I**). Subsequently, as illustrated in Fig. 2**e-II**, a hydroxide ion from water abstracts a second hydrogen, ultimately leading to the formation of the aldehyde (–CHO) group [38,70–72] (Fig. 2**f**).

The rapid conversion of FFCA to FDCA observed under O_2 in a biphasic MIBK/H_2O system (Table S7, entry 8) underscores the crucial role of water—not only provides hydroxide ions, but it also facilitates the desorption of FFCA, enabling complete oxidation. In contrast, when the reaction is carried out under O_2 in MIBK alone (Table S7, entry 10), FFCA is formed exclusively with only 9.5 % conversion, indicating that the absence of water hinders further oxidation. Similarly, under a N_2 atmosphere in the biphasic system (Table S7, entry 9), the reaction slows markedly. These results suggest that while hydroxide ions produced from water in the presence of AuNPs can drive limited oxidation—as observed in the initial HMF to HMFCA step—the synergistic effect of both ROS and hydroxide ions is necessary to achieve high yields of FDCA. This is consistent with recent findings on Au–ZrO_x catalysts, where oxygen vacancies and interfacial sites were shown to facilitate O_2 activation into ROS, accelerating the hydroxymethyl oxidation of HMFCA to FFCA — identified as the rate-determining step [62]. A similar conclusion was reached using $AuPdPt/TiO_2$@HNTs catalysts, where the oxidation of HMFCA was also identified as the limiting step, and enhanced ROS generation through multi-metal synergy and oxygen vacancies enabled high FDCA yields under mild conditions [73].

3.3.3. *Conversion of FFCA to FDCA*

The final step, the oxidation of FFCA to FDCA, mirrors the mechanism of HMF to HMFCA. The aldehyde group (–CHO) in FFCA adsorbs on a surface hydroxyl group, by interacting with the electrophilic carbon of the aldehyde group, followed by oxidation to a carboxylic acid group (–COOH) (Fig. 2**g-i**). The role of water is crucial in this process, as provides hydroxide ions and facilitates FDCA desorption from the catalyst surface. This is further supported by literature, where a study on the solubility of FDCA in various solvents reports that water has a higher solubility for FDCA than MIBK [74]. This enhanced solubility in water likely aids in the effective desorption of FDCA and supports the overall oxidation mechanism.

3.4. *Stability of the catalysts*

Besides activity and selectivity, stability is the third pillar of heterogeneous catalysis. To evaluate this property, the two most active catalysts—Au/HT_{Na} DP and Au/HT_{NH4} SI—were selected as representatives of the DP and SI methods, respectively.

The reusability of the Au/HT_{Na} DP and Au/HT_{NH4} SI catalysts was

evaluated over four consecutive reaction cycles, as shown in Fig. S3. For Au/HT_{Na} DP (Fig. S3a), a gradual decline in conversion and FDCA yield was observed in subsequent cycles. By the fourth cycle, the FDCA yield decreased to approximately 30 %, while the intermediate products, FFCA and HMFCA, began to accumulate. In contrast, the Au/HT_{NH4} SI catalyst (Fig. S3b) exhibited greater stability over the four cycles. The initial FDCA yield was 57 %, and while a slight reduction was observed in the later cycles, the catalyst maintained approximately 40 % FDCA yield by the fourth cycle. Furthermore, HMF conversion remained consistently high, with larger yields of the intermediate products compared to Au/HT_{Na} DP. These results indicate that while Au/HT_{Na} DP offers superior initial conversion and FDCA yield, its activity decreases more significantly over repeated uses. On the other hand, Au/HT_{NH4} SI demonstrates better stability, maintaining a more consistent activity throughout the cycles.

To understand the deactivation mechanisms, fresh and used catalysts were characterized through ICP analysis and Hammett titration. ICP data (Table S8) revealed progressive magnesium leaching in both catalysts. For Au/HT_{Na} DP, the Mg/Al ratio decreased from 2.4 in the fresh catalyst to 1.5 after the first use (36.2 % leaching), 1.07 after the third use (18.6 % leaching), and finally to 0.9 after the fourth use. A similar trend was observed for Au/HT_{NH4} SI, where the Mg/Al ratio dropped from 2.5 to 1.8 after the first use (29.3 % leaching), 1.3 after the third use (18.1 % leaching), and 1.1 after the fourth use. Minor fluctuations in the Au/Al ratio suggested possible redistribution of AuNPs but confirmed that gold remained firmly attached to the support. Interestingly, no gold leaching was observed in any of the catalysts, which is noteworthy given that gold leaching is a common issue in similar catalytic systems; for example, Au/$Mg(OH)_2$ catalysts have been reported to experience gold leaching as high as 10.4 wt% under similar reaction conditions [75].

Hammett titration results (Table S4) further corroborated the loss of catalyst basicity. For Au/HT_{Na} DP (Table S4, entry 6), the total basicity decreased from 1.17 to 0.19 mmol/g, with a similar reduction observed for Au/HT_{NH4} SI (Table S4, entry 7). This decline in basicity, associated with the loss of surface hydroxyl groups and magnesium leaching, suggests that the leached compound is primarily $Mg(OH)_2$. It is noteworthy that in the used catalysts, the medium basic sites—typically associated with Mg–O pairs [58]—are likely lost first due to magnesium leaching. This initial loss is then followed by a reduction in the weak basic sites, further diminishing the overall basicity. Table S4 (entries 6 and 7) clearly illustrates this sequential degradation.

Experimental tests confirmed that the leached Mg species lacked catalytic activity by their own, as no changes in conversion or product yield were observed when the catalyst was removed after the first hour (Fig. 3), confirming that the observed catalysis was heterogeneous. However, brucite was proposed to facilitate the deprotonation of hydroxyl groups, thereby accelerating their oxidation to diacid products. This promoter role of brucite was supported by experimental observations, including a significant reaction acceleration when it was used as a co-catalyst with the Au/HT_{Na} DP catalyst (Table S7, entry 4).

Moreover, reuse experiments revealed that reduced magnesium leaching correlated with lower FDCA production (Table S9), confirming the key role of weak basic sites, associated to $Mg(OH)_2$ in the reaction mechanism. One possible reason for magnesium leaching was the formation of the acid product (FDCA) and intermediates (HMFCA and FFCA), which lowered the pH of the reaction medium. This pH decrease destabilized the hydrotalcite structure [36], promoting further magnesium leaching.

To assess whether higher substrate loading could influence catalyst activity or accelerate support degradation, the effect of increasing HMF concentration was studied (from 40 to 160 g/L) while maintaining the HMF/catalyst ratio. As shown in Fig. S4, HMF conversion and FDCA yield remained consistently high (>95 %) across the entire concentration range, indicating that the catalyst remains highly active under more concentrated conditions. Furthermore, ICP analysis of the used catalysts (Table S10) revealed that magnesium leaching levels remained unchanged regardless of HMF concentration. These results indicate that higher FDCA concentrations, resulting from increased HMF loadings, led to greater magnesium leaching; however, the relative extent (percentage) of leaching remains constant as the FDCA:Mg ratio is maintained. Importantly, no gold leaching was detected at any HMF concentration, confirming that the AuNPs remain stably anchored to the hydrotalcite support even under intensified reaction conditions.

3.5. *Strategies for improving the reusability of the Au/HTNa DP catalyst*

3.5.1. *Au/HT_{Na} DP catalyst with $Mg(OH)_2$*

To enhance the reusability of the Au/HT_{Na} DP catalyst, $Mg(OH)_2$ was introduced as a co-catalyst (Fig. S5). As previously observed, the presence of brucite accelerated the reaction by facilitating the deprotonation of hydroxyl groups, promoting their oxidation to diacid products. In addition to this catalytic role, $Mg(OH)_2$ is intended to help maintain the basicity of the reaction medium, preventing the pH drop that

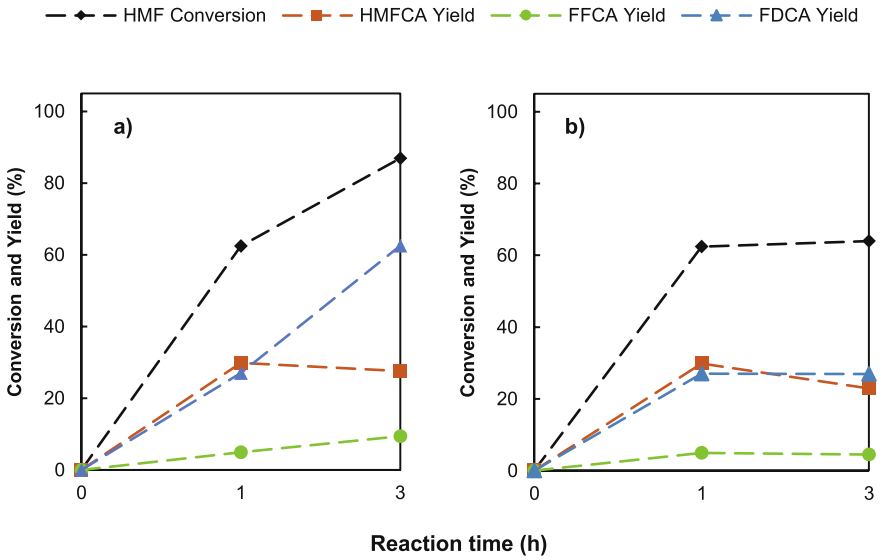

Fig. 3. Time course of product distribution. Reaction parameters: 3 bar (O_2), 95 °C, 500 rpm, 0.075 M HMF, 10 ml of total liquid phases, MIBK/H_2O volume ratio = 3:1: **a)** 0.06 g Au/HT; **b)** 0.06 g Au/HT and after 1 h, the catalyst was filtered off.

destabilizes the hydrotalcite structure.

However, activity tests revealed that this approach was not effective. As shown in Fig. S5a, a significant decline in catalytic activity was observed, indicating that the incorporation of $Mg(OH)_2$ did not enhance the structural stability. This was further corroborated by XRD analysis, which showed the degradation of the characteristic peaks of the hydrotalcitic phase (Fig. S5b). Notably, the XRD pattern of the used catalyst also exhibited peaks corresponding to $Mg_5(CO_3)_4(OH)_2(H_2O)_4$, suggesting that the carbonates present in the interlayer of the hydrotalcite may have reacted with the brucite, forming a new compound. These results suggest that the presence of $Mg(OH)_2$ was insufficient to preserve the layered structure of the catalyst, ultimately failing to prevent its deactivation. Some studies indicate that this strategy yields stable catalysts [76]. However, since these tests are performed at complete conversion, potential deactivation effects may go unnoticed. Similarly, reports of recyclable catalysts without an external base are based on 100 % conversion [41,77,78], suggesting that further evaluation under milder conditions is needed to fully assess long-term stability.

3.5.2. *Au/HT$_{Na}$ DP catalyst regeneration*

In order to enable the reusability of the Au/HT_{Na} DP catalyst caused by magnesium leaching during the oxidation of HMF to FDCA, a regeneration strategy using $Mg(OH)_2$ was implemented. As detailed in section 2.5, the regeneration procedure involved treating the used catalyst with a saturated $Mg(OH)_2$ solution under controlled conditions, followed by washing and drying steps. The addition of $Mg(OH)_2$ is supposed to serve a dual purpose: it reintroduces Mg^{2+} ions to help restore the hydrotalcite structure of the catalyst, and it replenishes the surface hydroxide basic sties that play a key role in the reaction mechanism.

This regeneration strategy proved to be effective. The regenerated Au/HT_{Na} DP catalyst recovered its initial catalytic activity. As illustrated in Fig. 4**a**, HMF conversion reached 92 %, with an FDCA yield of 74 %, values comparable to those of the fresh catalyst. XRD analysis was employed to observe structural changes in the fresh, used, and regenerated Au/HT_{Na} DP catalyst (Fig. 4**b**). After use in the oxidation of HMF, a reduction in peak intensity was observed, suggesting partial degradation of the layered structure, likely due to magnesium leaching and layer collapse. In the regenerated catalyst, peaks corresponding to the HT phase reappeared with intensities approaching those of the fresh catalyst, indicating substantial restoration of crystallinity. Additionally, new peaks corresponding to $Mg(OH)_2$ were detected, confirming its incorporation during regeneration. This is consistent with the high weak basicity observed in Table S4, entry 8, as $Mg(OH)_2$ mainly contributes to the recovery of weak basic sites. Meanwhile, the medium basic sites were only partially restored, suggesting that while the addition of brucite helps reestablish basicity associated to weak basic sites, the reformation of Mg–O pairs remains incomplete.

Furthermore, STEM-EDS analysis (Fig. 4**c-h**) provided deeper insight into the elemental distribution within the hydrotalcite structure. In both the fresh and regenerated catalysts, aluminum and magnesium were found to be homogeneously distributed, evidencing a uniform reintegration of Mg. In contrast, the used catalyst displayed a non-uniform Mg distribution, which did not correlate well with the Al mapping, highlighting the extent of Mg leaching. Importantly, no significant change in the AuNPs size or agglomeration was observed after regeneration, confirming that the process selectively restored the hydrotalcite structure without adversely affecting the dispersion of active gold sites. The basicity of the regenerated catalyst was determined using the Hammett titration method, with the results summarized in Table S4**,** entry 8. The analysis revealed notable differences in the total basicity and the distribution of basic sites among the fresh, used, and regenerated catalysts. Following regeneration, the catalyst exhibited a substantial recovery in basicity, reaching a total of 1.77 mmol/g with a pronounced increase in weak basic sites. This enhancement—surpassing the basicity of the fresh catalyst—can be attributed to structural modifications or the incorporation of new OH^- associated active sites during regeneration. These findings underscore the effectiveness of the regeneration strategy in not only restoring lost basicity but also in significantly increasing the catalyst's overall activity.

Additional insight into the regeneration mechanism was obtained via FTIR-ATR spectroscopy (Fig. S6a-c), which revealed changes in the carbonate and hydroxyl environments associated with the hydrotalcite structure. In the 1800–1200 cm^{-1} region (Fig. S6b), all samples exhibited characteristic bands attributable to interlayer carbonate species [79]. Notably, the regenerated catalyst showed a carbonate stretching band centered at 1361 cm^{-1}—shifted to higher wavenumbers compared to the fresh (1347 cm^{-1}) and used (1355 cm^{-1}) samples. This trend suggested an increase in the Mg/Al ratio and improved structural ordering following regeneration. Interestingly, the used sample exhibited slightly more intense and better-defined carbonate bands than the fresh catalyst. This may reflect local structural rearrangements or changes in carbonate coordination during catalytic operation, possibly due to partial dehydration or redistribution of interlayer species. Moreover, the FTIR spectra normalized to the 557 cm^{-1} band displayed broad asymmetric OH^- stretching bands across all samples in the 3700–2800 cm^{-1} region (Fig. S6c). The regenerated catalyst, showed a distinct shoulder at ~ 3078 cm^{-1}, which could be attributed to hydroxyl groups engaged in strong hydrogen bonding [80]— a feature also discernible in the fresh sample but absent in the used one. In summary, the spectra in Fig. S6a-c reflected a clear enhancement of both carbonate and OH-related vibrations in the regenerated sample. The presence of sharper bands, increased intensity, and frequency shifts consistent with higher crystallinity confirmed the successful reintegration of OH^- groups into the catalyst framework.

4. Conclusion

This study highlights the critical role of HT support composition and catalyst preparation methods in determining the activity and stability of Au/HT catalysts for HMF oxidation to FDCA. The Au/HT_{Na} DP catalyst achieved complete HMF conversion and 100 % FDCA yield without requiring an external base, with turnover frequencies of 12.1 h^{-1} (normalized by basic sites) and 287.4 h^{-1} (normalized by Au sites). The results demonstrate that the support precursor significantly influences the number and strength of weak basic sites—mainly surface OH^- groups—which, in combination with AuNPs, play a crucial role in governing the catalytic activity. Mechanistic insights reveal that the oxidation of HMF to FDCA proceeds via a three-step pathway, where surface hydroxyl groups play a key role in activating HMF through interactions with its electrophilic carbonyl group. Gold nanoparticles contribute by promoting oxygen activation to generate reactive oxygen species (ROS) and facilitating water activation to supply hydroxide ions, both essential for efficient oxidation. The biphasic MIBK/H_2O solvent system further enhances FDCA formation by stabilizing intermediates and facilitating their desorption from the catalyst surface.

Beyond activity, this work identifies magnesium leaching as the primary cause of catalyst deactivation, resulting in the loss of weak basic sites. A regeneration strategy employing $Mg(OH)_2$ was demonstrated to be effective in restoring both the structural integrity and catalytic performance of the material. This approach enables the long-term reuse of the catalyst under base-free conditions. These findings emphasize the importance of support composition and synthesis strategy not only in enhancing activity but also in ensuring stability. Furthermore, the mechanistic insights gained from this study provide valuable guidelines for the rational design of more durable and efficient catalysts for the sustainable production of FDCA and other bio-based chemicals.

Declaration of Generative AI and AI-assisted technologies in the writing process

During the preparation of this work the authors used ChatGPT in

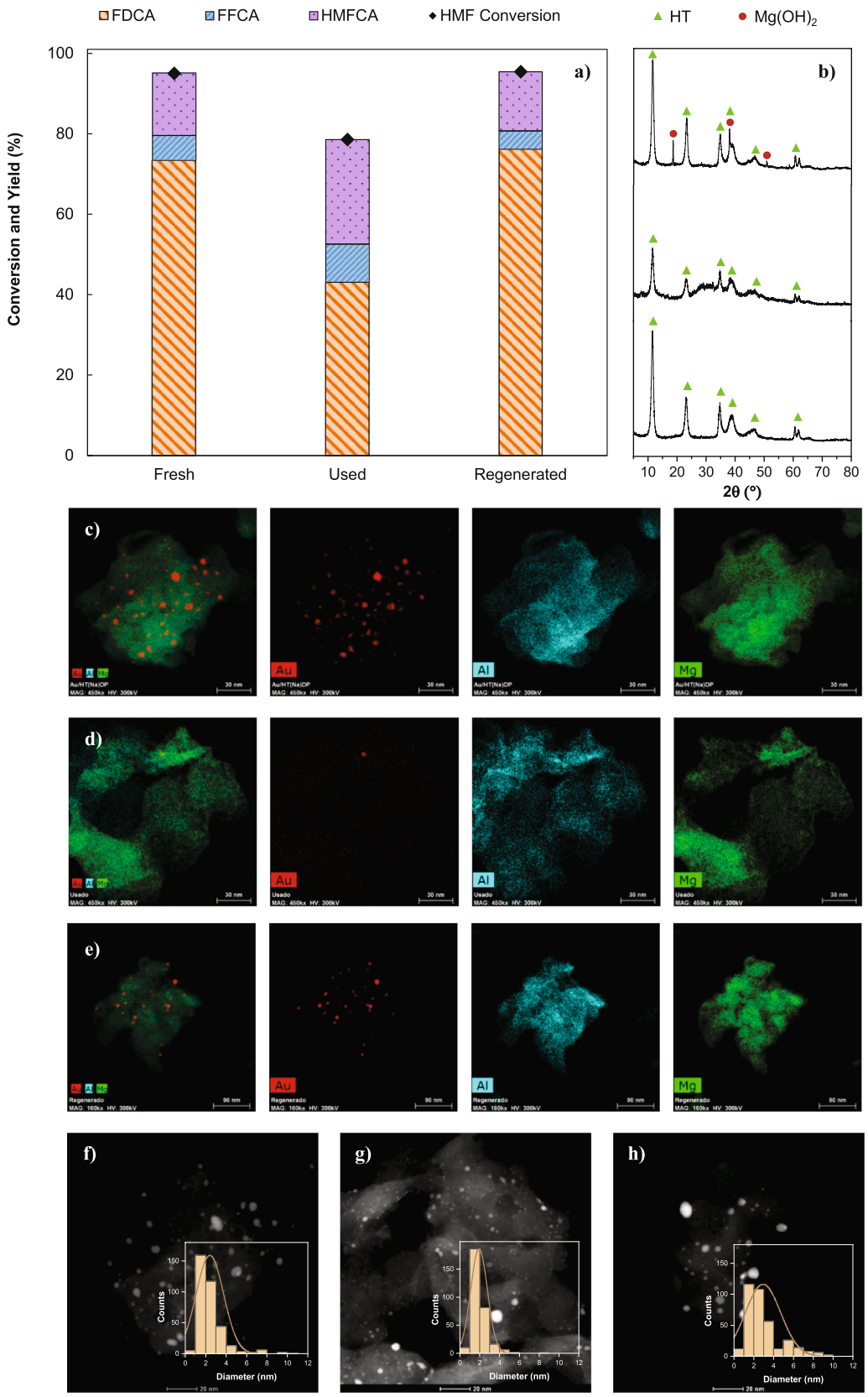

Fig. 4. **a)** HMF oxidation to FDCA over Au/HTNa DP catalyst during first, second, and regenerated use. Reaction parameters: 0.1 g HMF, 10 ml of total liquid phases, MIBK/H2O volume ratio = 3:1, 3 bar (O_2), 95°C, 500 rpm, 3 h, 0.17 g Au/HT_{Na} DP catalyst; **b)** XRD patterns of fresh, used and regenerated Au/HTNa DP catalyst. STEM-EDS elemental mapping of Au/HT_{Na} DP catalysts: **c)** fresh, **d)** used, and **e)** regenerated samples. TEM images and corresponding particle size distributions of **f)** fresh, **g)** used, and **h)** regenerated catalysts.

order to enhance the clarity and language of the manuscript. After using this tool, the authors reviewed and edited the content as needed and take full responsibility for the content of the publication.

CRediT authorship contribution statement

Ane Bueno: Writing – review & editing, Writing – original draft, Visualization, Validation, Resources, Methodology, Investigation, Conceptualization. **Nerea Viar:** Writing – review & editing, Writing – original draft, Visualization, Validation, Supervision, Methodology, Conceptualization. **Matthew B. Conway:** Visualization, Methodology, Investigation. **Inaki Gandarias:** Writing – review & editing, Validation, Supervision, Project administration, Methodology, Funding acquisition, Conceptualization. **Jesús M. Requies:** Writing – review & editing, Validation, Supervision, Project administration, Methodology, Funding acquisition, Conceptualization. **Meenakshisundaram Sankar:** Writing – review & editing, Visualization, Validation, Supervision, Methodology, Conceptualization.

Declaration of competing interest

The authors declare that they have no known competing financial interests or personal relationships that could have appeared to influence the work reported in this paper.

Acknowledgements

This research was supported by the University of the Basque Country (UPV/EHU), Basque Government (IT1554-22), and the Spanish Ministry of Economy, Industry and Competitiveness (PID2021-122736OB-C43). Ane Bueno also acknowledges support from the Basque Government through the "Ayudas nuevas para el Programa Predoctoral de Formación de Personal Investigador No Doctor", academic year 2023–2024, under the Investigación General category. MC and MS acknowledge the funding by the Engineering and Physical Sciences Research Council via the Prosperity Partnership EP/V056565/1 with bp and Johnson Matthey plc in collaboration with Cardiff University and the University of Manchester. XPS data collection was performed at the EPSRC National Facility for XPS (“HarwellXPS”), operated by Cardiff University and UCL, under Contract No. PR16195. The authors would like to thank the CCI-Electron Microscopy Facility which has been partially funded by the European Regional Development Fund through the Welsh Government and The Wolfson Foundation.

Appendix A. Supplementary material

Supplementary data to this article can be found online at https://doi.org/10.1016/j.fuel.2025.136088.

Data availability

Data will be made available on request.

References

[1] Rasheed T, Vattathurvalappil SH, Shaukat MM, Theravalappil R, Ali U, Ummer AC, et al. Recent updates on biodegradability and recyclability of bioplastics - towards a new era in sustainability. Sustain Mater Technol 2024;41.
[2] Hwang KR, Jeon W, Lee SY, Kim MS, Park YK. Sustainable bioplastics: recent progress in the production of bio-building blocks for the bio-based next-generation polymer PEF. Chem Eng J 2020;390.
[3] Wang B, Tu Z, Zhang X, Sang L, Chan W, Wang L, et al. New Advance in Biorenewable FDCA-Based Polyesters: Multiple Scale-up from Lab Bench to pilot Plant. Chem Eng J 2023;474:10.1016/j.cej.2023.145911.
[4] Min, J.; Tingting, L.; Qiang, Z.; Ying, C.; Guangyuan, Z. From Fossil Resources to Renewable Resources: Synthesis, Structure, Properties and Comparison of Terephthalic Acid-2 ,5-Furandicarboxylic Acid-Diol Copolyesters. In Proceedings of the Journal of Renewable Materials; Scrivener Publishing LLC, June 1 2015; Vol. 3, pp. 120–141.
[5] Aranha DJ, Gogate PR. A review on green and efficient synthesis of 5-hydroxymethylfurfural (HMF) and 2,5-Furandicarboxylic Acid (FDCA) from sustainable biomass. Ind Eng Chem Res 2022. https://doi.org/10.1021/acs.iecr.2c04047.
[6] Davidson MG, Elgie S, Parsons S, Young TJ. Production of HMF, FDCA and their derived products: a review of life cycle Assessment (LCA) and Techno-Economic Analysis (TEA) Studies. Green Chem 2021;23:3154–71. https://doi.org/10.1039/d1gc00721a.
[7] Van Putten RJ, Van Der Waal JC, De Jong E, Rasrendra CB, Heeres HJ, De Vries JG. Hydroxymethylfurfural, a Versatile Platform Chemical made from Renewable Resources. Chem Rev 2013;113:1499–597.
[8] Bueno, A.; Barredo, A.; Viar, N. Main Routes of Production of High-Value-Added 2,5-Furandincarboxylic Acid Using Heterogeneous Catalytic Systems. **2023**.
[9] Catalysts M, Yao Y, Wang G. Mechanism insights into the aerobic oxidation of 5-hydroxymethylfurfural mechanism insights into the aerobic oxidation of 5 – hydroxymethylfurfural to 2 , 5-furandicarboxylic acid over MnO 2. Catalysts 2021. https://doi.org/10.1021/acs.jpcc.0c09545.
[10] Milić M, Domínguez de María P, Kara S. A Patent Survey on the biotechnological production of 2,5-furandicarboxylic acid (FDCA). Current Trends and Challenges EFB Bioeconomy Journal 2023;3:100050. https://doi.org/10.1016/j.bioeco.2023.100050.
[11] Ardemani L, Cibin G, Dent AJ, Isaacs MA, Kyriakou G, Lee AF, et al. Solid base catalysed 5-HMF oxidation to 2,5-FDCA over Au/hydrotalcites: fact or fiction? Chem Sci 2015;6:4940–5. https://doi.org/10.1039/c5sc00854a.
[12] Rao M, Wang M, Zheng X, Pan D, Hong C, Chen K, et al. One-pot preparation of CuOx-CoOy heterostructure decorated on graphene for highly efficient oxidation of 5-hydroxymethylfurfural (5-HMF) to 2,5-furandicarboxylic acid (FDCA). Chem Eng Sci 2022;262. https://doi.org/10.1016/j.ces.2022.118004.
[13] Ayude MA, Doumic LI, Cassanello MC, Nigam KDP. Clean Catalytic oxidation for derivatization of key biobased platform chemicals: ethanol, glycerol, and hydroxymethyl furfural. Ind Eng Chem Res 2019;58:16077–95. https://doi.org/10.1021/acs.iecr.9b00977.
[14] Zeng D, Wang W, Cui B, Jiang B, Zhang C, Zhang L, et al. Base-free selective oxidation of 5-hydroxymethylfurfural to 2,5-furandicarboxylic acid over Au/MnO2 catalyst. Fuel 2025;381. https://doi.org/10.1016/j.fuel.2024.133238.
[15] Guan W, Zhang Y, Wei Y, Li B, Feng Y, Yan C, et al. Pickering HIPEs derived hierarchical porous nitrogen-doped carbon supported bimetallic AuPd catalyst for base-free aerobic oxidation of HMF to FDCA in water. Fuel 2020;278. https://doi.org/10.1016/j.fuel.2020.118362.
[16] Zhang Z, Deng K. Recent advances in the catalytic synthesis of 2,5-furandicarboxylic acid and its derivatives. ACS Catal 2015;5:6529–44.
[17] Xia H, Xu S, Hu H, An J, Li C. Efficient conversion of 5-hydroxymethylfurfural to high-value chemicals by chemo- and bio-catalysis. RSC Adv 2018;8:30875–86.
[18] Davis SE, Houk LR, Tamargo EC, Datye AK, Davis RJ. Oxidation of 5-Hydroxymethylfurfural over supported Pt Pd and Au catalysts. Catal Today 2011;160:55–60. https://doi.org/10.1016/j.cattod.2010.06.004.
[19] Zhang H, Zhang R, Zhang W, Gu B, Tang Q, Cao Q, et al. Base-free selective oxidation of 5-hydroxymethylfurfural over Pt nanoparticles on surface Nb-enriched Co-Nb oxide. Appl Catal B 2023;330. https://doi.org/10.1016/j.apcatb.2023.122670.
[20] Liu H, Zhang J, Li X, Zhang R, Jia W, Zhang J, et al. Strong electronic metal-support interaction between Ru nanoclusters and fe single atoms enables efficient base-free oxidation of 5-Hydroxymethylfurfural to 2,5-Furandicarboxylic Acid. Appl Catal B 2025;365. https://doi.org/10.1016/j.apcatb.2024.124994.
[21] Liu Y, Ma HY, Lei D, Lou LL, Liu S, Zhou W, et al. Active oxygen species promoted catalytic oxidation of 5-hydroxymethyl-2-furfural on facet-specific Pt nanocrystals. ACS Catal 2019;9:8306–15. https://doi.org/10.1021/acscatal.9b02115.
[22] Megías-Sayago C, Lolli A, Bonincontro D, Penkova A, Albonetti S, Cavani F, et al. Effect of gold particles size over Au/C catalyst selectivity in HMF oxidation reaction. ChemCatChem 2020;12:1177–83. https://doi.org/10.1002/cctc.201901742.
[23] Casanova O, Iborra S, Corma A. Biomass into chemicals: aerobic oxidation of 5-hydroxymethyl-2-furfural into 2,5-furandicarboxylic acid with gold nanoparticle catalysts. ChemSusChem 2009;2:1138–44. https://doi.org/10.1002/cssc.200900137.
[24] Schade OR, Kalz KF, Neukum D, Kleist W, Grunwaldt JD. Supported gold- and silver-based catalysts for the selective aerobic oxidation of 5-(hydroxymethyl) Furfural to 2,5-furandicarboxylic acid and 5-hydroxymethyl-2-furancarboxylic acid. Green Chem 2018;20:3530–41. https://doi.org/10.1039/c8gc01340c.
[25] Miao Z, Wu T, Li J, Yi T, Zhang Y, Yang X. Aerobic oxidation of 5-hydroxymethylfurfural (HMF) effectively catalyzed by a Ce0.8Bi0.2O2-δ supported Pt catalyst at room temperature. RSC Adv 2015;5:19823–9. https://doi.org/10.1039/c4ra16968a.
[26] Siyo B, Schneider M, Pohl MM, Langer P, Steinfelt N. Synthesis, characterization, and application of PVP-PD NP in the aerobic oxidation of 5-hydroxymethylfurfural (HMF). Catal Lett 2014;144:498–506. https://doi.org/10.1007/s10562-013-1186-0.
[27] Da Fonseca D, Ferreira A, Dorneles De Mello M, Da Silva MAP. Catalytic oxidation of 5-hydroxymethylfurfural to 2,5-furandicarboxylic acid over Ru/Al2O3 in a trickle-bed reactor. Ind Eng Chem Res 2019;58:128–37. https://doi.org/10.1021/acs.iecr.8b05602.
[28] Gorbanev YY, Klitgaard SK, Woodley JM, Christensen CH, Riisager A. Gold-catalyzed aerobic oxidation of 5-hydroxymethylfurfural in water at ambient temperature. ChemSusChem 2009;2:672–5. https://doi.org/10.1002/cssc.200900059.
[29] Pina, C. Della; Falletta, E.; Prati, L.; Rossi, M. Selective Oxidation Using Gold. Chem Soc Rev **2008**, 37, 2077–2095, doi:10.1039/b707319b.

[30] Chen B, Abe Y, Guo H, Lee Smith R. Selective oxidation of 5-hydroxymethylfurfural over MnOx-CeO2 catalyst prepared with Co-precipitation method. Fuel 2024;376. https://doi.org/10.1016/j.fuel.2024.132745.

[31] Xia H, An J, Hong M, Xu S, Zhang L, Zuo S. Aerobic oxidation of 5-hydroxymethylfurfural to 2,5-difurancarboxylic acid over Pd-Au nanoparticles supported on Mg-Al hydrotalcite. Catal Today 2019;319:113–20. https://doi.org/10.1016/j.cattod.2018.05.050.

[32] An J, Sun G, Xia H. Aerobic oxidation of 5-hydroxymethylfurfural to high-yield 5-hydroxymethyl-2-furancarboxylic acid by poly(vinylpyrrolidone)-capped Ag nanoparticle catalysts. ACS Sustain Chem Eng 2019;7:6696–706. https://doi.org/10.1021/acssuschemeng.8b05916.

[33] Jin M, Yu L, Chen H, Ma X, Cui K, Wen Z, et al. Base-free selective conversion of 5-hydroxymethylfurfural to 2,5-furandicarboxylic acid over a CoOx-CeO2 catalyst. Catal Today 2021;367:2–8. https://doi.org/10.1016/j.cattod.2020.10.038.

[34] Mani M, Mariyaselvakumar M, Tothadi S, Panda AB, Srinivasan K, Konwar LJ. Base free HMF oxidation over Ru-MnO2 catalysts revisited: evidence of Mn leaching to Mn-FDCA complexation and its implications on catalyst performance. Mol Catal 2024;554. https://doi.org/10.1016/j.mcat.2023.113811.

[35] Pasini T, Piccinini M, Blosi M, Bonelli R, Albonetti S, Dimitratos N, et al. Selective oxidation of 5-hydroxymethyl-2-furfural using supported gold–copper nanoparticles. Green Chem 2011;13:2091–9. https://doi.org/10.1039/c1gc15355b.

[36] Jobbágy M, Regazzoni AE. Dissolution of nano-size Mg-Al-Cl hydrotalcite in aqueous media. Appl Clay Sci 2011;51:366–9. https://doi.org/10.1016/j.clay.2010.11.027.

[37] Zope BN, Davis SE, Davis RJ. Influence of reaction conditions on diacid formation during Au-catalyzed oxidation of glycerol and hydroxymethylfurfural. Top Catal 2012;55:24–32. https://doi.org/10.1007/s11244-012-9777-3.

[38] Wang Y, Yu K, Lei D, Si W, Feng Y, Lou LL, et al. Basicity-tuned hydrotalcite-supported Pd catalysts for aerobic oxidation of 5-hydroxymethyl-2-furfural under mild conditions. ACS Sustain Chem Eng 2016;4:4752–61. https://doi.org/10.1021/acssuschemeng.6b00965.

[39] Choudhary H, Ebitani K. Hydrotalcite-supported PdPt-catalyzed aerobic oxidation of 5-hydroxymethylfurfural to 2,5-furandicarboxylic acid in water. Chem Lett 2016;45:613–5. https://doi.org/10.1246/cl.160178.

[40] Sun W, Gao T, Zhu G, Cao Q, Fang W. Influence of support properties and particle size on the gold-catalyzed base-free aerobic oxidation of 5-hydroxymethylfurfural. ChemistrySelect 2020;5:1416–23. https://doi.org/10.1002/slct.201904497.

[41] Gao T, Gao T, Fang W, Cao Q. Base-free aerobic oxidation of 5-hydroxymethylfurfural to 2,5-furandicarboxylic acid in water by hydrotalcite-activated carbon composite supported gold catalyst. Mol Catal 2017;439:171–9. https://doi.org/10.1016/j.mcat.2017.06.034.

[42] Gupta NK, Nishimura S, Takagaki A, Ebitani K. Hydrotalcite-supported gold-nanoparticle-catalyzed highly efficient base-free aqueous oxidation of 5-hydroxymethylfurfural into 2,5-furandicarboxylic acid under atmospheric oxygen pressure. Green Chem 2011;13:824–7. https://doi.org/10.1039/c0gc00911c.

[43] Takagaki A, Tsuji A, Nishimura S, Ebitani K. Genesis of catalytically active gold nanoparticles supported on hydrotalcite for base-free selective oxidation of glycerol in water with molecular oxygen. Chem Lett 2011;40:150–2. https://doi.org/10.1246/cl.2011.150.

[44] Fang W, Chen J, Zhang Q, Deng W, Wang Y. Hydrotalcite-supported gold catalyst for the oxidant-free dehydrogenation of benzyl alcohol: studies on support and gold size effects. Chem A Eur J 2011;17:1247–56. https://doi.org/10.1002/chem.201002469.

[45] Liu S, Zhu Y, Liao Y, Wang H, Liu Q, Ma L, et al. Advances in understanding the humins: formation, prevention and application. Appl Energy Combust Sci 2022;10. https://doi.org/10.1016/j.jaecs.2022.100062.

[46] Bueno A, Viar N, Barredo A, Gandarias I, Requies JM. Integrated PROCESS for 2,5-furandicarboxylic acid production from fructose via NaCl-promoted dehydration and Au/HT-catalyzed oxidation. J Ind Eng Chem 2025. https://doi.org/10.1016/j.jiec.2024.12.060.

[47] Van Der Lee MK, Van Jos Dillen A, Bitter JH, De Jong KP. Deposition precipitation for the preparation of carbon nanofiber supported nickel catalysts. J Am Chem Soc 2005;127:13573–82. https://doi.org/10.1021/ja053038q.

[48] Huang X, Akdim O, Douthwaite M, Wang K, Zhao L, Lewis RJ, et al. Au–Pd Separation enhances bimetallic catalysis of alcohol oxidation. Nature 2022;603:271–5. https://doi.org/10.1038/s41586-022-04397-7.

[49] Ahlers SJ, Bentrup U, Linke D, Kondratenko EV. An INNOVATIVE approach for highly selective direct conversion of CO2into propanol using C2H4and H2. ChemSusChem 2014;7:2631–9. https://doi.org/10.1002/cssc.201402212.

[50] Souzanchi S, Nazari L, Rao KTV, Tan (Chao) Z, Xu (Charles) C. Continuous isomerization of glucose to fructose using activated hydrotalcite catalyst: effects of reaction conditions. Appl Catalsis O: Open 2024;190:206954. https://doi.org/10.1016/j.apcato.2024.206954.

[51] Zhang T, Xu J, Sun Y, Fang S, Wu Z, Gao E, et al. Exploring the key components of Au Catalyst during CO oxidation using TG-MS and operando DRIFTS-MS. Mol Catal 2023;547. https://doi.org/10.1016/j.mcat.2023.113361.

[52] Kruse N, Chenakin S. XPS characterization of Au/TiO2 catalysts: binding energy assessment and irradiation effects. Appl Catal A 2011;391:367–76. https://doi.org/10.1016/j.apcata.2010.05.039.

[53] Socha RP, Zackiewicz E, Spiridis N, Korecki J. Au Adsorption on defect-Rich MgO (100) surfaces. In Proceedings of the Surface and Interface Analysis June 2010;42:536–9.

[54] Du Y, Hu R, Jia Y, Zhou Q, Meng W, Yang J. CuCl2 promoted low-gold-content Au/C catalyst for acetylene hydrochlorination prepared by ultrasonic-assisted impregnation. J Ind Eng Chem 2016;37:32–41. https://doi.org/10.1016/j.jiec.2016.02.011.

[55] Liu Y, Wei Z, Xing T, Lu M, Li X. Performance of Au/FeOx-TiO2 Catalyst for liquid phase Selective Hydrogenation of Phthalic Anhydride to Phthalide. J Ind Eng Chem 2015;23:321–7. https://doi.org/10.1016/j.jiec.2014.08.036.

[56] Villa A, Wang D, Veith GM, Vindigni F, Prati L. Sol Immobilization technique: a delicate balance between activity, selectivity and stability of gold catalysts. Cat Sci Technol 2013;3:3036–41. https://doi.org/10.1039/c3cy00260h.

[57] Drault F, Snoussi Y, Ferraz CP, Thuriot-Roukos J, Heyte S, Junior II, et al. Versatility of supported gold nanoparticles on hydrotalcites used for oxidation and reduction reactions. Catalysis Research 2021;2:1. https://doi.org/10.21926/cr.2201001.

[58] Zeng HY, Xu S, Liao MC, Zhang ZQ, Zhao C. Activation of reconstructed Mg/Al hydrotalcites in the transesterification of microalgae oil. Appl Clay Sci 2014;91–92:16–24. https://doi.org/10.1016/j.clay.2014.02.003.

[59] Cai J, Ma H, Zhang J, Song Q, Du Z, Huang Y, et al. Gold nanoclusters confined in a supercage of Y zeolite for aerobic oxidation of HMF under mild conditions. Chem A Eur J 2013;19:14215–23. https://doi.org/10.1002/chem.201301735.

[60] Albonetti S, Lolli A, Morandi V, Migliori A, Lucarelli C, Cavani F. Conversion of 5-hydroxymethylfurfural to 2,5-furandicarboxylic acid over Au-based catalysts: optimization of active phase and metal-support interaction. Appl Catal B 2015;163:520–30. https://doi.org/10.1016/j.apcatb.2014.08.026.

[61] Kim M, Su Y, Fukuoka A, Hensen EJM, Nakajima K. Aerobic oxidation of 5-(Hydroxymethyl)furfural cyclic acetal enables selective furan-2,5-dicarboxylic acid formation with CeO 2 -supported gold catalyst. Angew Chem 2018;130:8367–71. https://doi.org/10.1002/ange.201805457.

[62] Zhang Y, Cao Y, Yan C, Liu W, Chen Y, Guan W, et al. Rationally designed Au-ZrOx interaction for boosting 5-hydroxymethylfurfural oxidation. Chem Eng J 2023;459. https://doi.org/10.1016/j.cej.2023.141644.

[63] Li Q, Wang H, Tian Z, Weng Y, Wang C, Ma J, et al. Selective oxidation of 5-hydroxymethylfurfural to 2,5-furandicarboxylic acid over Au/CeO2 catalysts: the morphology effect of CeO2. Cat Sci Technol 2019;9:1570–80. https://doi.org/10.1039/c9cy00211a.

[64] Sang B, Li J, Tian X, Yuan F, Zhu Y. Selective aerobic oxidation of the 5-hydroxymethylfurfural to 2,5-furandicarboxylic acid over gold nanoparticles supported on graphitized carbon: study on reaction pathways. Mol Catal 2019;470:67–74. https://doi.org/10.1016/j.mcat.2019.03.026.

[65] Megías-Sayago C, Lolli A, Ivanova S, Albonetti S, Cavani F, Odriozola JA. Au/Al2O3 – efficient catalyst for 5-hydroxymethylfurfural oxidation to 2,5-furandicarboxylic acid. Catal Today 2019;333:169–75. https://doi.org/10.1016/j.cattod.2018.04.024.

[66] Albonetti S, Pasini T, Lolli A, Blosi M, Piccinini M, Dimitratos N, et al. Selective oxidation of 5-hydroxymethyl-2-furfural over TiO 2-supported gold-copper catalysts prepared from preformed nanoparticles: effect of Au/Cu ratio. Catal Today 2012;195:120–6. https://doi.org/10.1016/j.cattod.2012.05.039.

[67] Dononelli W, Tomaschun G, Klüner T, Moskaleva LV. Understanding oxygen activation on nanoporous gold. ACS Catal 2019;9:5204–16. https://doi.org/10.1021/acscatal.9b00682.

[68] Liu Z, Tan Y, Li J, Li X, Xiao Y, Su J, et al. Ag substituted Au clusters supported on Mg-Al-hydrotalcite for highly efficient base-free aerobic oxidation of 5-hydroxymethylfurfural to 2,5-furandicarboxylic acid. Green Chem 2022;24:8840–52. https://doi.org/10.1039/d2gc02775e.

[69] Daté M, Haruta M. Moisture effect on CO oxidation over Au/TiO2 Catalyst. J Catal 2001;201:221–4. https://doi.org/10.1006/jcat.2001.3254.

[70] Davis SE, Zope BN, Davis RJ. On the Mechanism of selective oxidation of 5-hydroxymethylfurfural to 2,5-furandicarboxylic acid over supported Pt and Au catalysts. Green Chem 2012;14:143–7. https://doi.org/10.1039/c1gc16074e.

[71] Davis SE, Ide MS, Davis RJ. Selective oxidation of alcohols and aldehydes over supported metal nanoparticles. Green Chem 2013;15:17–45.

[72] Lolli A, Albonetti S, Utili L, Amadori R, Ospitali F, Lucarelli C, et al. Insights into the reaction mechanism for 5-hydroxymethylfurfural oxidation to FDCA on bimetallic Pd-Au nanoparticles. Appl Catal A 2015;504:408–19. https://doi.org/10.1016/j.apcata.2014.11.020.

[73] Zhang Y, Liu Y, Xia Q, Chen Y, Kong L, Yan X, et al. Ambient temperature catalyzed air-oxidation of 5-hydroxymethylfurfural via ternary metal and oxygen vacancies. Green Energy Environ 2025. https://doi.org/10.1016/j.gee.2025.02.003.

[74] Zhang Y, Guo X, Tang P, Xu J. Solubility of 2,5-furandicarboxylic acid in eight pure solvents and two binary solvent systems at 313.15-363.15 K. J Chem Eng Data 2018;63:1316–24. https://doi.org/10.1021/acs.jced.7b00927.

[75] Cai C, Xu J, Wang H, Xin H, Zhang Q, Wang C, et al. Homogeneous base-free oxidation of 5-hydroxymethyfufural to 2, 5-furandicarboxylic acid over Au/Mg(Oh)2 catalysts. ChemistrySelect 2020;5:12785–90. https://doi.org/10.1002/slct.202003408.

[76] Takagaki A, Takahashi M, Nishimura S, Ebitani K. One-Pot Synthesis of 2,5-Diformylfuran from Carbohydrate Derivatives by Sulfonated Resin and Hydrotalcite-Supported Ruthenium Catalysts. ACS Catal 2011;1:1562–5. https://doi.org/10.1021/cs200456t.

[77] Gao D, Fang F, Waterhouse GIN, Han F, Li YSP. Modified CoFe-LDH derived CoFeS and CoFeP-400 catalysts efficiently catalyze the oxidation of HMF to FDCA. Cat Sci Technol 2024;14:1191–200. https://doi.org/10.1039/d4cy00010b.

[78] Kumar R, Lee HH, Chen E, Du YP, Lin CY, Prasanseang W, et al. Facile synthesis of the atomically dispersed hydrotalcite oxide supported copper catalysts for the

selective hydrogenation of 5–hydroxymethylfurfural into 2,5-bis(hydroxymethyl) furan. Appl Catal B 2023;329. https://doi.org/10.1016/j.apcatb.2023.122547.
[79] Frost RL, Spratt HJ, Palmer SJ. Infrared and near-infrared spectroscopic study of synthetic hydrotalcites with variable divalent/trivalent cationic ratios. Spectrochim Acta A Mol Biomol Spectrosc 2009;72:984–8. https://doi.org/10.1016/j.saa.2008.12.018.
[80] Gueta R, Natan A, Addadi L, Weiner S, Refson K, Kronik L. Local atomic order and infrared spectra of biogenic calcite. Angewandte Chemie - International Edition 2007;46:291–4. https://doi.org/10.1002/anie.200603327.